

Phase separation from electron confinement at oxide interfaces

N. Scopigno¹, D. Bucheli¹, S. Caprara^{1,2}, J. Biscaras³, N. Bergeal³, J. Lesueur³, and M. Grilli^{1,2}

¹*Dipartimento di Fisica, Università di Roma “La Sapienza”, P.le Aldo Moro 5, 00185 Roma, Italy*

²*ISC-CNR and Consorzio Nazionale Interuniversitario per le Scienze Fisiche della Materia, Unità di Roma “Sapienza” and*

³*Laboratoire de Physique et d’Etude des Matériaux - CNRS-ESPCI ParisTech-UPMC,*

PSL Research University, 10 Rue Vauquelin - 75005 Paris, France.

(Dated: May 24, 2022)

Oxide heterostructures are of great interest both for fundamental and applicative reasons. In particular the two-dimensional electron gas at the LaAlO₃/SrTiO₃ or LaTiO₃/SrTiO₃ interfaces displays many different physical properties and functionalities. However there are clear indications that the interface electronic state is strongly inhomogeneous and therefore it is crucially relevant to investigate possible intrinsic electronic mechanisms underlying this inhomogeneity. Here the electrostatic potential confining the electron gas at the interface is calculated self-consistently, finding that the electron confinement at the interface may induce phase separation, to avoid a thermodynamically unstable state with a negative compressibility. This provides a generic robust and intrinsic mechanism for the experimentally observed inhomogeneous character of these interfaces.

PACS numbers: 73.20.-r, 73.43.Nq, 73.21.Fg, 74.81.-g

The two-dimensional electron gas (2DEG) that forms at the interface of two insulating oxides, like LaAlO₃/SrTiO₃ and LaTiO₃/SrTiO₃ (hereafter generically referred to as LXO/STO) [1–4], exhibits a rich phenomenology, such as a gate-tunable metal-to-superconductor transition [5–8], a magnetic-field-tuned quantum criticality [9], and inhomogeneous magnetic responses [10–15]. Tunneling [16, 17] and SQUID magnetometry [18] provide clear evidence of an inhomogeneous interface on both micro- and nanoscopic scales. Transport measurements report further signs of inhomogeneity and a percolative metal-to-superconductor transition with a sizable fraction of the 2DEG never becoming superconducting down to the lowest accessible temperatures [19–22]. For both fundamental reasons and applicative purposes, like device design, it is crucial to identify possible *intrinsic* mechanisms that may render the 2DEG so strongly inhomogeneous via a phase separation (PS). This is precisely the focus of the present work.

Here, we identify a very effective electron-driven mechanism leading to PS, based on the confinement of the 2DEG at the interface. From customary self-consistent calculations of the confining potential well in semiconductors, it is well known [23] that a finite lateral extension usually renders the 2DEG more compressible than its strictly 2D counterpart. This effect is much stronger in LXO/STO than in ordinary semiconductor interfaces, due to the huge dielectric constant of STO, allowing for much larger electron densities, with a strong amplification of the self-consistent adjustments of the confining potential. As a consequence, a non-rigid band structure arises, which varies with the local electron density: an increased electron density is accompanied by a corresponding increase of the positive countercharges (due to oxygen vacancies and/or polarity catastrophe [24–29]), from which the interfacial electrons are introduced and restoring the overall charge neutrality. For small-to-moderate

increases of electron and countercharge densities the potential well deepens and the electron energy levels are shifted downwards. In this Letter we show that this mechanism leads *by itself* to PS.

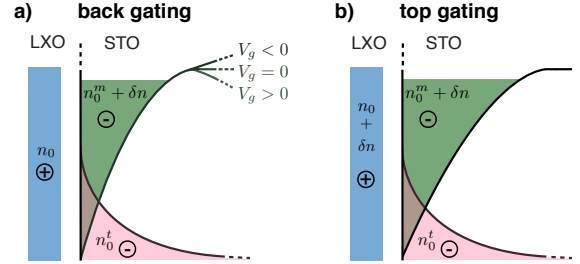


FIG. 1. Sketch of the interface for back (a) and top (b) gating. The confining potential depends on both mobile (n_0^m) and trapped (n_0^t) charges. Applying a positive (negative) voltage, δn electrons per unit cell are added to (subtracted from) the interface and the potential changes accordingly.

— *The model* — The thermodynamic stability of the system is investigated by varying the density of the interfacial gas *while keeping the overall neutrality*. Therefore a corresponding amount of positive countercharges has to be varied (see Fig. 1). Due to this tight connection between positive and negative charges the (in)stability will be determined by calculating the chemical potential of the whole system (i.e., of both the mobile electrons and of the rest of the charges). While for the electron part we will solve the quantum problem of the mobile electrons in the self-consistent confining well, the countercharges, the fraction of electrons trapped in impurity states of the bulk (see below) and the boundary conditions fixing the gating potential will determine the classical electrostatic energy of the system. We will keep all these contributions (for a detailed description see the Appendix) into account to calculate the total energy \mathcal{E} and, in turn, the

chemical potential $\mu = \mathcal{E}(N+1) - \mathcal{E}(N) \approx \partial_N \mathcal{E}$ (here N represents the number of electrons, which is always kept equal to the number of countercharges).

The energy of the 2DEG is obtained through the calculation of the energy spectra as a function of the electron density, $n \equiv \delta n + n_0$ [henceforth, carrier densities, e.g., n , carrying no z dependence are meant per interfacial unit cell (u.c.), and are related to their z -dependent counterparts by relations like, e.g., $n = \int_0^\infty dz n(z)$]. Here, the two contributions have different origin: δn is the extrinsic component introduced by gating, while the intrinsic component n_0 [30] originates from the electronic reconstruction due to the polarity catastrophe and/or from oxygen vacancies within the LXO layer. Which of the two dominates is not important in our calculations and we represent the related positive countercharges as the light-blue shaded areas in the LXO side of Fig. 1.

What matters, instead, is the way the extrinsic charges are introduced, particularly in the case of back-gating [Fig. 1 (a)]: Applying a positive voltage V_g , the electrostatic potential, after increasing in the region close to the interface, decreases linearly with distance, once the interfacial charge density has been exhausted [the electrons reside on the STO side, which we assume to occupy the $z > 0$ half space and $n(z) \rightarrow 0$ for large z]. Then the electrons closest to the top of the well are weakly confined and some of them may escape and get trapped into the defects of bulk STO, as it is demonstrated by irreversibility effects under large back-gating potentials [31]. Thus in the absence of trapped charges, the quantum well is intrinsically unstable upon positive back-gating. In the top-gating configuration [Fig. 1 (b)], the leakage also occurs, because the Fermi energy of the electrons, attracted to the interface by the positive V_g , exceeds the confining potential on the STO side. In both configurations, we are therefore led to introduce trapped charges that we describe by a distribution $n_0^t(z) = (n_0^t/\lambda)e^{-z/\lambda}$ on the STO side, decaying over a distance λ of several tens of nanometers (see pink shaded area in Fig. 1). This has the main effect of deepening the confining potential well, the Fermi energy being located substantially below its top (see, e.g., Refs. 8 and 32).

The mobile electrons occupy energy levels that are quantized in the z direction and form a 2D band structure in the xy (interfacial) plane. The electrostatic potential $\phi(z)$ confining the electrons is determined self-consistently with the mobile electron density distribution $n^m(z) \equiv n_0^m(z) + \delta n(z)$ (at external gating V_g), for a frozen distribution of trapped charges $n_0^t(z)$. The z component of the factorized wave function $\Psi(x, y, z) = \zeta(z)\psi_{k_x k_y}(x, y)$ is the solution of the Schrödinger equation yielding the sub-band energy ε_i ,

$$\left[\frac{\hbar^2}{2m_\alpha^z} \frac{d^2}{dz^2} + e\phi(z) + \varepsilon_{i\alpha} \right] \zeta_{i\alpha}(z) = 0, \quad (1)$$

where the electron charge is $-e$ and $i = 1, 2, 3, \dots$ is the

sub-band index. The index $\alpha = xy, xz, yz$ labels the three Ti t_{2g} orbitals, d_{xy}, d_{xz}, d_{yz} , where the electron mostly reside. The full 2D band structure is

$$\varepsilon_{i,\alpha,\mathbf{k}} = \frac{\hbar^2 k_x^2}{2m_\alpha^x} + \frac{\hbar^2 k_y^2}{2m_\alpha^y} + \Delta_\alpha + \varepsilon_{i\alpha}.$$

Taking $\Delta_{xy} = 0$, the energy offset $\Delta_{xz,yz} \equiv \Delta$ of the $d_{xz,(yz)}$ bands is experimentally found to be $\Delta \approx 50$ meV [34]. Similar values are found in first-principle calculations between the highest occupied d_{xy} sub-band and the lowest $d_{xz,yz}$ sub-bands [35]. Here we have to adjust $\Delta \approx 0 - 10$ meV in order to self-consistently obtain the energy difference between the d_{xy} and the $d_{xz,yz}$ sub-bands of order 50 – 60 meV (see the Appendix), showing that the energy offset mostly arises from the different mass along the z direction. We take the masses of the various bands as $m_{xy}^{x,y} = m_l$, $m_{xy}^z = m_h$; $m_{xz}^{x,z} = m_l$, $m_{xz}^y = m_h$; $m_{yz}^{y,z} = m_l$, $m_{yz}^x = m_h$. According to standard values [36], we take $m_l = 0.7 m_e$ and $m_h = 14 m_e$ (m_e is the electron mass). Assuming full translational invariance along the xy planes and integrating over a u.c. of area a^2 with a suitable normalization of $\psi_{k_x k_y}(x, y)$, the density of mobile electrons, at temperature $T = 0$, reads

$$n^m(z) = \sum_{i\alpha} |\zeta_{i\alpha}(z)|^2 \int_{-\infty}^{\varepsilon_F} d\varepsilon g_{i\alpha}(\varepsilon),$$

where $g_{i\alpha}(\varepsilon) = a^2 (\pi \hbar^2)^{-1} \sqrt{m_\alpha^x m_\alpha^y} \theta(\varepsilon - \varepsilon_{i\alpha} - \Delta_\alpha)$ is the density of states (DOS) of the various t_{2g} sub-bands, $\theta(\varepsilon)$ is the Heaviside function, and ε_F is the Fermi energy.

The electron distribution corresponds to an electrostatic potential $\tilde{\phi}(z)$ obeying the Poisson equation:

$$\frac{\epsilon_0 a^2}{e} \frac{d}{dz} \left[\epsilon_r(E) \frac{d}{dz} \tilde{\phi}(z) \right] = n^m(z) + n_0^t(z). \quad (2)$$

Here, the dielectric constant is a function of the electric field $E = -d\tilde{\phi}/dz$ via the relation $\epsilon_r(E) = (A + B|E|)^{-1} + \epsilon_\infty$, where A , B , and ϵ_∞ are experimentally measured constants [37]. Owing to the nearly ferroelectric character of STO, ϵ_r can reach very large values ($\gtrsim 25 \times 10^3$) but, due to the very strong interfacial electric field [8, 38], we find that, near $z = 0$, $\epsilon_r \approx \epsilon_\infty \approx 100 - 300$. The crucial point of the above derivation is that the calculation is self-consistent only if the two potentials, ϕ from Eq. (4) and $\tilde{\phi}$ from Eq. (5), coincide.

Besides the difficulties stemming from the self-consistency, there are additional subtleties coming from the boundary conditions, which vary for the back- or top-gating configuration. In the former case we fix a density of positive charges $n_0 = \int_0^\infty dz [n_0^m(z) + n_0^t(z)]$ (per u.c.) at $z = 0^-$. We made this simplifying choice, which turns out to be slightly less favorable to the occurrence of PS, to avoid the distinction between the case of oxygen vacancies (for which the countercharge would be uniformly

distributed in the LXO) and the polarity catastrophe (in which the countercharges suitably distribute themselves in the polar planes of LXO in order to minimize the energy [39]). Having fixed the positive charges, we consider the electric field at $z = 0^+$ (i.e., the slope of the confining potential) at the interface. The electric field deep inside the STO [where $n_0(z) \rightarrow 0$] is fully determined by the gate potential because the intrinsic electronic density and the corresponding positive charges in the LXO compensate and have thus no effect in this region. On the other hand, the electrons coming from back-gating create a field V_g/L , with $e\delta n = \epsilon_0 a^2 \int_0^{V_g/L} \epsilon_r(E) dE$, where L is the thickness of the STO substrate. In the top-gating configuration, instead, the density of positive charges at $z = 0^-$ amounts to $n_0 + \delta n$, and the electric field vanishes deep inside the STO substrate.

Once the quantum problem of mobile electrons is solved, the rest of the energy is due to the electrostatic contribution (per u.c.) of electric fields due to the overall distribution of the mobile (m) and the fixed (f , from gates and trapped) charges

$$\mathcal{E}_{es} = \frac{\epsilon_0 a^2}{2} \int_{-\infty}^{\infty} \epsilon_r(E) [E^f{}^2(z) - E^m{}^2(z)] dz, \quad (3)$$

with $E = E^f + E^m$. Notice that, since the Hartree-like electrostatic energy is double-counted in the quantum Hamiltonian, the contribution of the mobile charges must be subtracted in Eq. (3). In the Appendix we provide details of how the above fields are calculated.

— *Results* — To evidenciate that the electron confinement is the driving mechanism of PS we first consider the pure quantum problem neglecting the classical electrostatic contributions to the free energy. We thus report in Fig 2(a) the evolution of the different sub-bands levels as a function of the mobile electron density n^m , which is the sum of the initial as grown carrier density n_0^m and the extra charges δn added by electrostatic gating. This evolution is a direct consequence of the non-rigidity of the bands. The resulting Fermi energy E_F is going up as expected, while the chemical potential μ^m of the mobile electrons has a non-monotonic behavior. Indeed, when E_F crosses the first heavy band ($d_{xz,yz}$ which have the largest DOS along the $x - y$ plane), μ^m starts to decrease. The most important result of this paper is that, for a given range of mobile electron densities, the chemical potential decreases while electrons are added, resulting into a negative compressibility. The entailed thermodynamic instability is prevented by PS, with the consequent inhomogeneous redistribution of electrons and countercharges. Remarkably, the electron system tends to stay unstable (i.e. it has a negative compressibility) up to very large densities showing that this instability mechanism is strong and robust. However, this cannot be a physical situation, since the compressibility remains negative, preventing a stable phase separation to occur.

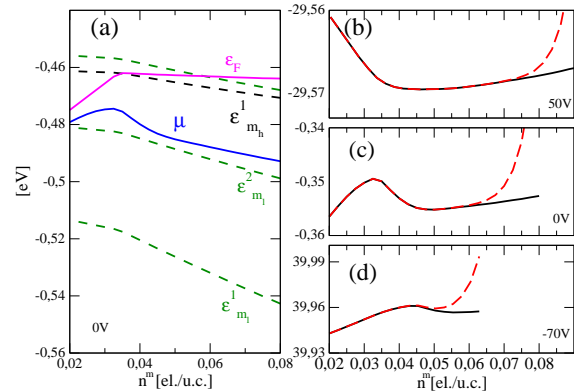


FIG. 2. (a) Fermi energy (magenta solid line), electron-only (see text) chemical potential (blue solid line), sub-band levels (green dashed for the d_{xy} and black dashed for the $d_{xz,yz}$ levels) as a function of the build-in density n_0 at zero gating potential. (b) Chemical potential as a function of the mobile electron density $n^m = n_0^m + \delta n$ at fixed values of the back gating potential $V_g \propto \delta n$ (the δn electrons due to gating are thus also fixed). The black solid (red dashed) lines correspond to the solution in the absence (presence) of a countercharge background with short-range rigidity. The short-range background contribution to the chemical potential is taken of the form $\mu_{sr}(n^m) = A[(n^m - \delta n)/0.065]^p$, where the exponent $p = 19$ measures the short-range rigidity and $A = 7 \times 10^{-4}$. For $V_G = 50$ V, $\delta n = 0.013668$. (c) Same as (b) with $\delta n = 0$. (d) Same as (b) with $\delta n = -0.01711$.

Indeed, this model is not complete. One has to introduce the energetic cost of the electrostatic fields generated by all the charges in the system according to Eq.(3). This leads to the chemical potential displayed in the panels of Fig. 2 (b-d) (black solid line) when n^m is increased (the gate voltage is kept constant in this calculation, while the intrinsic n_0^m is varied).. Taking into account the quantum and electrostatic energies restores a physical situation, where the negative compressibility occurs in a limited range of doping, since for high n^m , μ increases when adding carriers.

Now the increasing classic electrostatic energy cost tend to stabilize the system at large n_0^m and allow to perform a standard Maxwell construction on the μ vs. n^m curves at each gate potential. The resulting phase diagram is shown in Fig 3) for back [Fig 3(a)] and top [Fig 3(b)] gate. The dashed orange lines limit the stability region (in between the system is phase separated), corresponding to the densities n_1 and n_2 . We also plot the gate voltage as a function of n_m (blue solid lines) for different samples having different densities at zero gating.

As can be seen in Fig. 3 the "miscibility gap" remains open at very negative gate voltage, especially in the back-voltage configuration. This does not correspond to the

experimental situations [?]. This discrepancy arises because, while we took into account the long-range electrostatic cost of the charge distribution, we did not include in our model any short range repulsion between the countercharges (oxygen vacancies or positive charges left by the polarity catastrophe reconstruction). While some mild fluctuations of electrons and compensating countercharges are accepted, when too many electrons would segregate carrying along too large densities of countercharges, the system becomes very rigid and the charge segregation stops.

To overcome this problem, we added a short-range repulsion to the total energy. Of course a precise estimate of the energy involved in these repulsive interactions is out of reach for the present calculations and we only implement a phenomenological energy barrier that induces a rapid grow in $\mu(n)$ when electron densities above those experimentally found (with a maximum of 0.5 el/u.c., including the trapped charges) is reached. Due to this additional short-range mechanism, the PS region determined by the Maxwell construction on the dashed red lines of Figs. 2 (b-d) is reduced (black solid lines and squares in Fig. 3) and, quite remarkably, it ends with a critical point at some critical negative gate value, V_g^c . The resulting phase diagram for back-gating is reported in Fig. 3(a). The initial (as-grown) density n_0 is determined by several specific parameters (like, e.g., the number of LXO planes). Starting from a given n_0 , the total density per u.c., $n = n_0 + \delta n$, is then changed by the gating following the thin blue trajectories in the phase diagram. Inspection of these trajectories reveals a very large range of intrinsic densities n_0 leading to PS. Upon increasing the negative gating the overall average density n decreases and the fraction of the system with lower density n_1 increases, in agreement with transport measurements [21, 22, 40], until the system exits the PS region at some negative voltage. A similar behavior is found for the top-gating case whose phase diagram is reported in Fig. 3(b).

— *Discussion* — From Figs. 3 (a) and (b) one can see that there exists a broad range of the intrinsic density n_0 yielding a negative compressibility, prevented by PS. This PS yields an inhomogeneous 2DEG with associated inhomogeneity of the oxygen vacancies and/or electronic reconstructions. We carried out a detailed analysis (see also the Appendix) to identify the specific mechanisms determining this instability finding that it arises from two main features peculiar to these oxide interfaces.

First of all, the electrons at the interface are confined in the STO side where a large dielectric constant ($\epsilon_r > \epsilon_\infty \gtrsim 100$) efficiently screens the electric fields. This allows for the accommodation of a large number of electrons ($\approx 10^{13} \text{ cm}^{-2}$) on several confined levels. The large DOS coming from the contributions of the individual sub-bands greatly enhances the electron compressibility and facilitates the instability. This effect is stronger

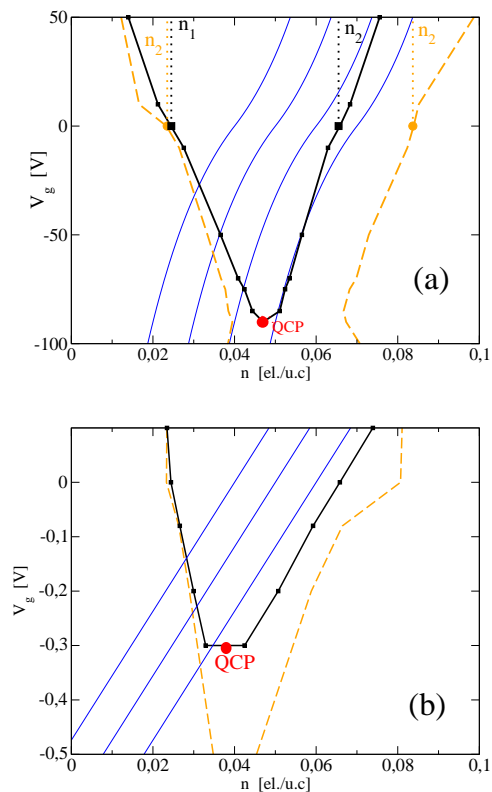


FIG. 3. (a) Gate potential versus mobile electron density phase diagram for the back gated LXO/STO interface in the absence (orange dashed lines) and in the presence (black solid lines) of short-range rigidity of the countercharges. n_1 and n_2 are determined by the Maxwell construction. The blue thin solid lines correspond to $n_0 = 0.04, 0.05, 0.06, 0.07$ el/u.c. at $V_g = 0$. (b) Same as (a) for the top-gating case, with $n_0 = 0.04, 0.05, 0.06$ el/u.c.

when $d_{xz,yz}$ sub-bands start to be filled because they have a rather large DOS. The relevance of the d_{xz}, d_{yz} levels has already been asserted in Hartree-Fock calculations [41] and seems to be experimentally supported [42]. The filling of these levels typically starts when the system enters the PS dome upon increasing V_g , and rapidly leads to increasingly more abundant regions with locally higher electron density. We speculate that this corresponds to the observed increase of high-mobility carriers and onset of superconductivity [8, 21].

Secondly, a larger n_0 must correspond to larger density of countercharges on the LXO side, which attracts the interface electrons and deepens the confining potential well, causing a downward shift of the quantized levels.

Interestingly, in a rather large range of n_0 values, the system exits the PS dome in the vicinity of the critical point located here at $n_0^c \approx 0.0475$ el/u.c. and $V_g^c \approx -70$ V for back-gating (see blue line trajectories in Fig.3). This suggests that decreasing V_g the electrons in the LXO/STO interface eventually display some sig-

natures of critical behavior where superconductivity will likely be affected by the strong quantum density fluctuations [43].

In conclusion, we identified a mechanism of electron-driven PS. While the details of the phase-separated region also depend on the short-range rigidity of the system, the existence and robustness of the PS is on a firm ground and can be responsible for the strong inhomogeneity observed at LXO/STO interfaces. This mechanism can also cooperate with other intrinsic [38] or extrinsic (e.g., defects or domain walls [18, 44]) mechanisms.

We thank V. Brosco, C. Castellani, R. Raimondi, and G. Seibold for stimulating discussions. We acknowledge financial support from the Sapienza University Project n. C26A115HTN, the CNRS PICS program ‘‘S2S’’, the ANR JCJC ‘‘Nano-SO2DEG’’, the SESAME, OXY-MORE and CNano programs from R egion IdF.

APPENDIX

Numerical calculation of the self-consistent electronic well

A well-tested approach to an eigenvalue problem in electronic quantum wells at the interface of two semiconductors is reported in [45]. It consist in the simultaneous solution of the coupled Poisson and Schr odinger (in the effective mass approximation) equations

$$\left[\frac{\hbar^2}{2m_z} \frac{d^2}{dz^2} + e\phi(z) + \varepsilon_i \right] \zeta_i(z) = 0, \quad i = 1, 2, 3, \dots \quad (4)$$

$$\frac{\epsilon_0 a^2}{e} \frac{d}{dz} \left[\epsilon_r(E) \frac{d}{dz} \phi(z) \right] = n(z) \quad (5)$$

which gives us both the eigenfunctions and the confining potential well. The close analogies between semiconductors and oxides heterointerfaces allows us to apply this method to the LXO/STO potential as well. The boundary conditions for the set (4)-(5) can be understood considering the schematic picture of the interface shown in fig. (4). Within this approach, the electric field and the displacement field are by symmetry only directed along the z axis. Therefore henceforth we will indicate with E and D only the z components of the fields.

The energy gap between the LXO and STO conduction bands is about $3eV$, so that in the low-filling regime it is safely to approximate the potential step at the LXO/STO interface as an infinite energy barrier. In addition the eigenfunctions have to be normalizable, therefore we are led to set of boundary conditions

$$\zeta_i(0) = 0 \quad \zeta_i(\infty) = 0. \quad (6)$$

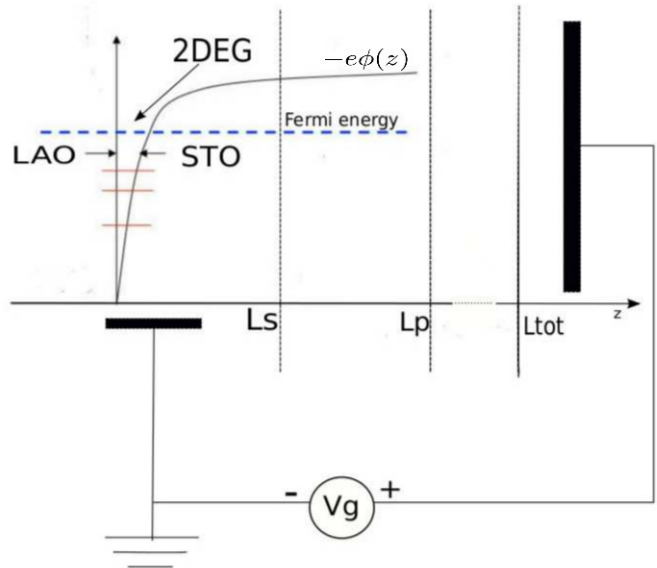


FIG. 4. Schematic view of the back-gating configuration in LAO/STO.

The second condition can be implemented numerically exploiting the fact we are dealing with a confining potential: in a region far enough from the interface the eigenfunctions are exponentially decreasing. If L_S resides in that region, the set (6) can be replaced by

$$\zeta_i(0) = 0 \quad \zeta_i(L_S) = 0. \quad (7)$$

The boundary conditions for the Poisson equation depend on both the (positive) countercharges left in the LXO valence band and on the gating voltage. Experimental evidences show that the width of the 2DEG is only few nanometers, while the trapped charges extend over a few tens of nanometers [8, 31]. If L_P is the thickness of the region in which all the charge is confined we can solve the Poisson equation analytically in the interval (L_P, L_{TOT}) and find appropriate boundary conditions by the reasoning reported below. We take $L_P = 100nm$, that is large enough to study also long-tail distributions of the trapped charges.

Let us consider the interval $[0^-, +\infty)$: in this region the system is neutral and we can reasonably impose the condition

$$E(-\infty) = E(+\infty) = 0 \quad (8)$$

on the electric field, for any gating potential V_G . In $[0^+, +\infty)$ the neutrality does no longer hold, because the positive charges (left at the interface of LXO by the polar catastrophe or homogeneously distributed in the LXO layer if they are given by the oxygen vacancies) are now excluded. Thus the electric field verifies the condition

$$\int_{0^+}^{+\infty} dz \frac{d}{dz}(\epsilon_r E) = +\frac{n_0}{\epsilon_0} \Rightarrow \epsilon_r(0^+)E(0^+) = -\frac{n_0}{\epsilon_0} \quad (9)$$

where n_0 are the polar catastrophe charges and we have used Eq. (8) to cancel the term $\epsilon_r(+\infty)E(+\infty)$. Since all the electronic charges (mobile $n^m = n_0^m + \delta n$, and trapped n_0^t) are between 0^+ and L_P , the electric field in $z \in (L_P, L_{TOT})$ is uniform even for the non linear experimental form of the relative dielectric constant $\epsilon_r = (A + B|E|)^{-1} + \epsilon_\infty$ [A , B and ϵ_∞ are experimentally measured constants [37]]. The boundary value for the potential thus reads

$$\phi(L_P) = \frac{V_g}{L_{TOT}} L_P, \quad (10)$$

where V_g is the external gating.

Numerical solution

Because of the nonlinear behavior of (4)-(5), an analytic approach is not viable and we adopted a numerical iterative procedure to performs the calculation through the following steps:

- The starting point is the potential at the n th iteration, $\phi_n(z) = \phi_{old}^n(z)$, and his derivative, the electric field $E_n(z) = E_{old}^n(z)$, $z \in [0, L_S]$. We solve Eq. (4) using a Finite Element Method (FEM) algorithm [46], finding the energies ϵ_i and the eigenfunctions ζ_i which verify the conditions (7). We recall that L_S has to be taken far enough from the interface to ensure that the eigenfunctions are in a region in which they have an evanescent behavior. This can be done choosing different values for L_S and checking them *a posteriori*. The envelope functions are normalized imposing the condition $\int_0^{L_S} |\zeta_i(z)|^2 dz = 1$.
- From the knowledge of the eigenvalues, the Fermi level can be calculated inverting numerically (e.g, using a bisection method) the relation $n^m = \int_{-\epsilon_0}^{\epsilon_F} g(\epsilon) d\epsilon$, and from $n^m(z) = \sum_i |\zeta_i(z)|^2 \int_{-\infty}^{\epsilon_F} d\epsilon g_i(\epsilon)$ we have the density profile along z of the 2DEG. Here only the mobile electrons contribute to define the Fermi energy since the trapped charges reside in impurity levels, deep or localized enough to be safely considered as a stable quenched charge distribution.
- The profile of the potential well is found once one knows both the distribution of the 2DEG and the trapped (negative) charges. While the first is calculated self-consistently, the second is fixed at the zeroth step. There are no experimental evidences

that determine univocally the distribution of the trapped charges, but a reasonable choice is a decreasing exponential distribution of the form

$$n_0^t(z) = \left(\frac{n_0^t}{\lambda}\right) e^{-\frac{z}{\lambda}}. \quad (11)$$

Its shape is controlled by two parameters: the decay length λ and the maximum value n_0^t/λ .

- The Poisson equation is solved in the interval $[0^+, L_P]$. This gives a new potential $\phi(z) = \phi_{new}^n(z)$ and a new electric field $E(z) = E_{new}^n(z)$.
- The update at the next step is performed defining the quantities

$$\begin{aligned} \phi_{n+1}(z) &= s\phi_{old}^n(z) + (1-s)\phi_{new}^n(z) \\ E_{n+1}(z) &= sE_{old}^n(z) + (1-s)E_{new}^n(z) \end{aligned}$$

where the parameter $s \in [0, 1]$ is used to control the difference between the old potential and the new one; this reduces the risk that the iterative procedure escapes from the self-consistent solution and does not converge. The calculation stops as soon as the condition

$$\int_0^{L_P} |\phi_{n+1} - \phi_n|^2 dz < \delta \quad (12)$$

is fulfilled, for a suitably chosen accuracy δ .

Through the previous five steps we obtain the potential well $V(z) = -e\phi(z)$ (with the corresponding Fermi energy ϵ_F), the electric field $E(z)$ and the density $n^m(z)$ of the 2DEG for a given value of n_0 .

In principle the numerical solution may depend on the choice of the error δ in (12), the initial potential $\phi_0(z)$ and the discretization length (according to the standard FEM [46], we discretized in N_{elem} intervals the region in which we solve the Schrödinger equation). We performed different tests to ensure the reliability of the numerical solution. In order to exclude the dependence on the initial potential, we varied the initial condition ϕ_0 in a reasonable class of functions and kept n_0 and V_g fixed. We find that the numerical solution is stable with respect to the initial data. N_{elem} and δ has been fixed to reach the uniform convergence. The solution is almost independent of δ while the choice of the first parameter is critical to obtain the uniform convergence. In our work we took N_{elem} so that $\sup_{n_0} |\epsilon_F(N_{elem} + 1) - \epsilon_F(N_{elem})|$ is of order $\approx 10^{-5}$, a suitable request to reduce the error under the typical variations ($\sim 10^{-3} eV$) of the chemical potential $\mu(n)$.

Electrostatic energy

While the previous section solved the quantum problem of electrons in a self-consistent potential, here we provide details of the calculation of the other electrostatic contributions to the total energy of the system arising from the fixed charges (those on the gating electrodes and the charges trapped in the impurity states inside the STO) and from the mobile charges at the interface.

We consider two possible gating configurations. For the back-gating, the near region is the interval $z \in [0, L_p]$, while the far region is the $z \in (L_p, L_{tot})$ interval. On the other hand, for the top-gating, while the so-called near region is the same, the “far” region corresponds to the LXO side of the heterostructure and corresponds to the $z \in [-d, 0)$ interval.

In the near region we solve the Poisson equation

$$\frac{d}{dz}D(z) = n^m(z) + n_0^t(z) \quad (13)$$

to find the electric displacement field $D(z) = D^m(z) + D^f(z)$ due to the mobile and fixed charges. In this region the only fixed charges are those trapped in the STO side, while the charges on the electrodes and the countercharges on the LXO side only enter as boundary conditions. The electric field is

$$E = \frac{-\text{sgn}(D)[1 + \epsilon_\infty A - \text{sgn}(D)BD]}{2B\epsilon_0\epsilon_\infty} \quad (14)$$

$$+ \frac{\sqrt{[1 + \epsilon_\infty A - \text{sgn}(D)BD]^2 + \text{sgn}(D)4\epsilon_\infty ABD}}{2B\epsilon_0\epsilon_\infty}$$

The total electric displacement field is obtained by numerically integrating Eq.(13), while the field due to the fixed charges is analytically found from

$$\frac{d}{dz}D^f(z) = n_0^t(z). \quad (15)$$

The result is

$$D^f(z) = -\frac{en_0^t}{2a^2}(1 - 2e^{-\frac{z}{\lambda}}) + \frac{en_0}{2a^2} - \frac{e\delta n}{2a^2} \quad (16)$$

Once D and D^f are known, the electric displacement due to the mobile charges is obtained from $D^m = D - D^f$. The electric fields of the fixed and mobile charges are

$$E^{f,m} = \frac{D^{f,m}}{\epsilon_0} \frac{A + B|E|}{1 + \epsilon_\infty(A + B|E|)}. \quad (17)$$

Notice that the non-linearity of ϵ_r entails the dependence of $D^{f,m}$ and $E^{f,m}$ on the total electric field E given by Eq.(14)

In the far region we have different expressions for the top- and back-gating configurations. For the latter the

far region coincides with the bulk of the STO substrate, where

$$D^m(z) = \frac{en_0^t}{2a^2} - \frac{e\delta n}{2a^2} - \frac{en_0}{2a^2} \quad (18)$$

$$D^f(z) = -\frac{en_0^t}{2a^2} + \frac{en_0}{2a^2} - \frac{e\delta n}{2a^2} \quad (19)$$

are constant. The corresponding electric fields are then obtained by solving Eqs.(14) and (17).

The far region in the top-gating configuration is instead given by the whole LXO side, where the dielectric constant ϵ_{LXO} is really constant

$$E^m(z) = \frac{e\delta n}{2\epsilon_0\epsilon_{LXO}a^2} - \frac{en_0^t}{2\epsilon_0\epsilon_{LXO}a^2} + \frac{en_0}{2\epsilon_0\epsilon_{LXO}a^2} \quad (20)$$

$$E^f(z) = \frac{e\delta n}{2\epsilon_0\epsilon_{LXO}a^2} + \frac{en_0^t}{2\epsilon_0\epsilon_{LXO}a^2} - \frac{en_0}{2\epsilon_0\epsilon_{LXO}a^2} \quad (21)$$

-
- [1] A Ohtomo and H. Y. Hwang, Nature (London) **427**, 423 (2004)
 - [2] J. Mannhart, D. H. A. Blank, H. Y. Hwang, A. J. Millis, and J. M. Triscone, MRS Bulletin **33**, 1027 (2008).
 - [3] J. Mannhart and D. G. Schlom, Science **327**, 1607 (2010).
 - [4] H. Y. Hwang, Y. Iwasa, M. Kawasaki, B. Keimer, N. Nagaosa, and Y. Tokura, Nat. Mat. **11**, 103 (2012).
 - [5] N. Reyren, S. Thiel, A. D. Caviglia, L. Fitting Kourkoutis, G. Hammerl, C. Richter, C. W. Schneider, T. Kopp, A.-S. Retschi, D. Jaccard, M. Gabay, D. A. Muller, J.-M. Triscone, and J. Mannhart, Science **317**, 1196 (2007).
 - [6] D. Caviglia, S. Gariglio, N. Reyren, D. Jaccard, T. Schneider, M. Gabay, S. Thiel, G. Hammerl, J. Mannhart, and J.-M. Triscone, Nature (London) **456**, 624 (2008).
 - [7] J. Biscaras, N. Bergeal, A. Kushwaha, T. Wolf, A. Rastogi, R. C. Budhani, and J. Lesueur, Nat. Commun., DOI: 10.1038, and arXiv:1002.3737.
 - [8] J. Biscaras, N. Bergeal, S. Hurand, C. Grossetête, A. Rastogi, R. C. Budhani, D. LeBoeuf, C. Proust, J. Lesueur, Phys. Rev. Lett. **108**, 247004 (2012).
 - [9] J. Biscaras, N. Bergeal, S. Hurand, C. Feuillet-Palma, A. Rastogi, R. C. Budhani, M. Grilli, S. Caprara, and J. Lesueur, Nat. Mat. **12**, 542 (2013).
 - [10] Ariando, X. Wang, G. Baskaran, Z. Q. Liu, J. Huijben, J. B. Yi, A. Annadi, A. Roy Barman, A. Rusydi, S. Dhar, Y. P. Feng, J. Ding, H. Hilgenkamp, and T. Venkatesan, Nat. Commun. **2**, 188 (2011).
 - [11] Lu Li, C. Richter, J. Mannhart, and R. C. Ashoori, Nat. Phys. **7**, 762 (2011).
 - [12] J. A. Bert, B. Kalisky, C. Bell, M. Kim, Y. Hikita, H. Y. Hwang, and K. A. Moler, Nat. Phys. **7**, 767 (2011).
 - [13] D. A. Dikin, *et al.*, Phys. Rev. Lett. **107**, 056802 (2011).
 - [14] M. M. Mehta, D. A. Dikin, C. W. Bark, S. Ryu, C. M. Folkman, C. B. Eom, and V. Chandrasekhar, Nat. Commun. **3**, 955 (2012).
 - [15] J. A. Bert, K. C. Nowack, B. Kalisky, H. Noad, J. R. Kirtley, C. Bell, H. K. Sato, M. Hosoda, Y. Hikita, H. Y. Hwang, K. A. Moler, Phys. Rev. B **86**, 060503(R) (2012).

- [16] C. Richter, *et al.*, Nature (London) **502**, 528 (2013).
- [17] D. Bucheli, S. Caprara, and M. Grilli, arXiv:1405.4666v1.
- [18] B. Kalisky, *et al.*, Nature Mat. **12**, 1091 (2013).
- [19] S. Caprara, M. Grilli, L. Benfatto, and C. Castellani, Phys. Rev. B **84**, 014514 (2011).
- [20] D. Bucheli, S. Caprara, C. Castellani, and M. Grilli, New J. Phys. **15**, 023014 (2013).
- [21] S. Caprara, J. Biscaras, N. Bergeal, D. Bucheli, S. Hurand, C. Feuillet-Palma, A. Rastogi, R. C. Budhani, J. Lesueur, and M. Grilli, Phys. Rev. B **88**, 020504(R) (2013).
- [22] S. Caprara, D. Bucheli, M. Grilli, J. Biscaras, N. Bergeal, S. Hurand, C. Feuillet-Palma, J. Lesueur, A. Rastogi, and R. C. Budhani, SPIN **4**, 1440004 (2014).
- [23] J. P. Eisenstein, L. N. Pfeiffer, and K. W. West, Phys. Rev. B **50**, 1760 (1994).
- [24] The origin of the interfacial electrons is still controversial. Besides the electronic reconstruction mechanism related to the polarity catastrophe [25], the occurrence of oxygen vacancies is widely considered and controversial[26–28]. See also [29] and references therein.
- [25] N. Nakagawa, H. Y. Hwang, and D. A. Muller, Nat. Mat. **5**, 204 (2006).
- [26] Y. Chen, *et al.*, Nano Letters **11**, 3774 (2011).
- [27] G. De Luca, *et al.*, Appl. Phys. Lett. **104**, 261603 (2014)
- [28] E. Di Gennaro, *et al.*, Sci. Rep. **5**, 8393 (2015).
- [29] Liping Yu and Alex Zunger, Nat. Commun. **5**, 5118 (2014).
- [30] The gate potential V_g (and the associated density δn) are external parameters determining the thermodynamic state of the system. In contrast, the density n_0 and its fluctuations are determined by the internal stability of the system. Thus, establishing whether for a given value of n_0 , say n_0^{exp} (fixed by the chemistry of the sample), the 2DEG is stable or not, amounts to determine whether the chemical potential is an increasing or a decreasing function of n_0 in the vicinity of n_0^{exp} , while keeping $V_g \propto \delta n$ fixed.
- [31] J. Biscaras, S. Hurand, C. Feuillet-Palma, A. Rastogi, R. C. Budhani, N. Reyren, E. Lesne, J. Lesueur, and N. Bergeal, Sci. Rep. **4**, 6788 (2014).
- [32] W. Meevasana, P. D. C. King, R. H. He, S-K. Mo, M. Hashimoto, A. Tamai, P. Songsirittthigul, F. Baumberger, and Z-X. Shen, Nat. Mater. **10**,114 (2011).
- [33] D. Bucheli, M. Grilli, F. Peronaci, G. Seibold, and S. Caprara, Phys. Rev. B **89**, 195448 (2014).
- [34] M. Salluzzo, *et al.* Phys. Rev. Lett. **102**, 166804 (2009).
- [35] Z. Zhong, A. Tóth, and K. Held, Phys. Rev. B **87**, 161102(R) ...
- [36] A. F. Santander-Syro, *et al.*, Nature **469**, 189 (2011).
- [37] R. Neville, C. Mead, and B. Hoeneise, J. Appl. Phys. **43**, 2124 (1972).
- [38] S. Caprara, F. Peronaci, and M. Grilli, Phys. Rev. Lett. **109**, 196401 (2012).
- [39] Kevin Steffen, Florian Loder, and Thilo Kopp Phys. Rev. B **91**, 075415 (2015).
- [40] S. Caprara, D. Bucheli, N. Scopigno, N. Bergeal, J. Biscaras, S. Hurand, J. Lesueur, and M. Grilli, Supercond. Sci. Technol. **28**, 014002 (2015).
- [41] Se Young Park and Andrew J. Millis, Phys. Rev. B **87**, 205145 (2013).
- [42] Arjun Joshua, S. Pecker, J. Ruhman, E. Altman and S. Ilani, Nat. Commun. **3**, 1129 (2012).
- [43] S. Caprara, N. Bergeal, J. Lesueur, and M. Grilli, arXiv:1503.05997
- [44] N. C. Bristowe, T. Fix, M. G. Blamire, P. B. Littlewood, and E. Artacho, Phys. Rev. Lett. **108**, 166802 (2012).
- [45] F. Stern, and W. E. Howard, Phys. Rev. Lett. **163**, 3 (1967)
- [46] L.R. Ram-Mohan, *Finite Element and Boundary Element Applications in Quantum Mechanics*, Oxford University Press.